Stacking-Specificity of Surface Plasmon Polaritons

in Trilayer Graphene

Boogeon Choi[1], Gyouil Jeong[1], Seongjin Ahn[2], Hankyul Lee[1], Yunsu Jang[2], Baekwon Park[1],

Hans A. Bechtel[3], Byung Hee Hong[1], Hongki Min[2], and Zee Hwan Kim[1]*

[1]Department of Chemistry, Seoul National University, 08826, Seoul, Korea`

[2]Department of Physics and Astronomy, Seoul National University, 08826, Seoul, Korea

[3]Advanced Light Source Division, Lawrence Berkeley National Laboratory, Berkeley,

California 94720, USA

Abstract

We employed infrared scattering-type scanning near-field optical microscopy (IR-sSNOM) to study the impact of stacking order in TLG on surface plasmon polaritons (SPPs). Our study reveals systematic differences in near-field IR spectra and SPP wavelengths between Bernal (ABA) and rhombohedral (ABC) TLG domains on SiO_2, which can be explained by stacking-dependent intraband conductivities. We also observed that the SPP reflection profiles at ABA-ABC boundaries could be mostly accounted for by an idealized boundary defined by the conductivity discontinuity. However, we identified distinct shapes in SPP profiles at the edges of the ABA and ABC TLG, which cannot be solely attributed to idealized edges with differing conductivities. Instead, this disparity can be explained by the presence of stepped edge structure or the stacking-specific electronic edge states. Our findings unveil a new structural element that can control SPP, and provide insights into the structures and electronic states of edges of few-layer graphene.

1. Introduction

The infrared (IR) surface-plasmon polariton (SPP) of graphene[1-12] has garnered significant interest due to its potential to tightly confining the electromagnetic field to the material and enabling electrostatic control of its propagation characteristics. Effective control of SPP reflection is vital for realizing the ultimate flatland optoelectronic circuit. Previous experimental and theoretical studies have demonstrated that the edges of monolayer graphene (MLG) exhibit near-perfect reflection, independent of doping or environmental factors[1, 6, 13-15]. Other graphene nanostructures, such as topological domain walls[3, 5, 7, 15, 16], defects[1, 8, 15], and nano-gaps[17, 18] of MLG and bilayer graphene (BLG), also exhibit strong SPP reflections. However, such structures do not offer systematic control over SPP reflections. One promising approach for the control is the use of graphene heterojunction, where adjacent graphene domains possess distinct optical conductivities. This allows for electrical manipulation of the conductivity discontinuity at the junction, enabling control over SPP reflection and transmission. While several theoretical studies have explored the use of graphene junctions[19-21], experimental realizations remain limited.

Employing the IR scattering-type scanning near-field optical microscopy and spectroscopy (IR-sSNOM) at $\lambda_0 \sim 10$ μm, we studied the SPPs in Bernal (ABA) and rhombohedral (ABC) stacking domains of trilayer graphene (TLG). The stacking domains and their boundaries in few-layer graphene (FLG)[5, 22-29] provide a versatile platform for manipulating SPP reflection. Specifically, differently stacked domains of the doped FLG exhibit distinct intraband optical conductivities[30, 31]. Consequently, the domain boundaries can be utilized as controllable SPP reflectors, *provided* that the conductivity change across the boundaries follows a simple step-function defined by the conductivities of the adjacent domains.

2

We found that the near-field spectra and SPP wavelengths of TLG on SiO_2 substrate exhibit systematic stacking dependences, which can be fully explained by the stacking-specific intraband conductivities. We also observed that the SPP reflection profiles at ABA-ABC boundaries can be explained by an ideal boundary defined by the conductivity discontinuity, with the domain wall conductivity playing a marginal role. However, we identified distinct shapes in SPP profiles at the edges of the ABA and ABC TLG, which cannot be solely attributed to idealized edges with a spatially uniform conductivities of ABA and ABC domains. Rather, they can be explained by the edge with non-uniform conductivity profile, which indicates the presence of stepped edge structure or the stacking-specific electronic edge states. The result reveals a new structural component of graphene that can regulate the reflection of SPPs. Furthermore, it demonstrates a means to explore the structure and property of edges of few-layer graphene.

2. Methods

The TLG sample used in this study was obtained by mechanically exfoliating Kish-graphite and transferring it onto a SiO_2 (thickness of 285 nm) / Si substrate. The identification of ABA and ABC domains in TLG was achieved through Raman spectra (Supporting Information 1) and IR-sSNOM image contrasts at $\lambda_0 = 3.39$ μm (2950 cm^{-1}; further details provided below). Two IR-sSNOM setups (Figure 1a) were employed for the study: for the near-field spectroscopy, the setup at the Advanced Light Source (ALS) in Lawrence Berkeley National Lab, USA, utilizing a broadband synchrotron-generated IR continuum[32, 33]; for imaging, the setup at SNU[22, 34], employing a narrow-band IR-HeNe laser at 2950 cm^{-1} ($\lambda_0 = 3.39$ μm) and tunable quantum cascade lasers at 934 cm^{-1}~1000 cm^{-1} (QCLs, $\lambda_0 = 10.0 \sim 10.7$ μm). In both setups (Fig 1a), an oscillating atomic force microscopy (AFM) tip located above

3

the sample was illuminated with a focused IR radiation through a reflective focusing element (an off-axis parabolic mirror or a Cassegrain-type objective lens). The same optical element collected back-scattered radiation, and the scattered light was detected interferometrically using a Michelson interferometer and an IR-detector (HgCdTe or InSb). To eliminate far-field background, the tip was vertically oscillated near the natural frequency of the cantilever, and the lock-in filtered signal at the 2nd harmonic frequency of the tip oscillation was processed to give scattering intensity ($|s_2|^2$) and the scattering phase (ϕ_2). To model the optical conductivities, we employed tight-binding (TB) calculation[35] with parameters of intralayer hopping $\gamma_0 = 3.16$ eV, interlayer hopping $\gamma_1 = 0.39$ eV, and broadening by impurity $\eta = 40$ meV. The Kubo formula[22, 36, 37] was used to evaluate the intraband conductivities (Supporting Information 2).

4

3. RESULTS AND DISCUSSION

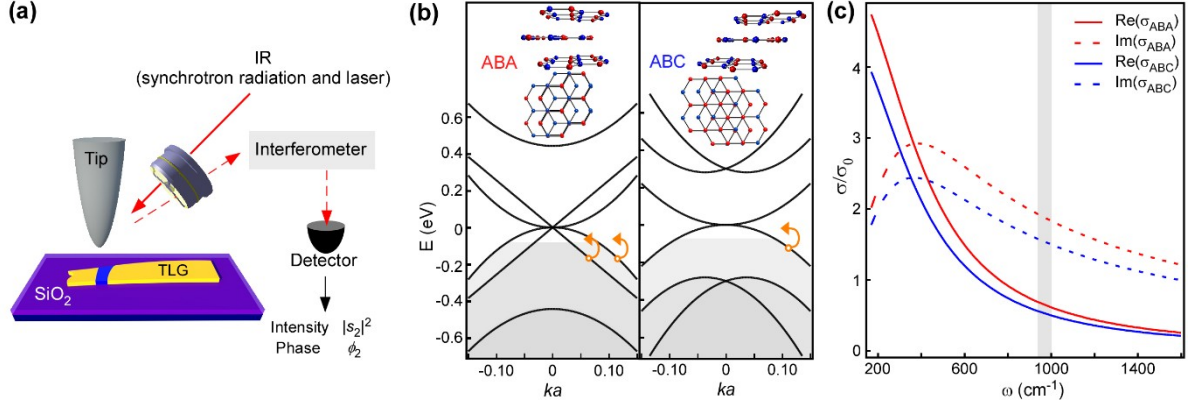### 3.1. Stacking-specific intraband optical conductivities

Figure 1. (a) Schematic of IR-sSNOM. (b) The crystal structures of Bernal (ABA) and rhombohedral (ABC) stacking domains of TLG and the corresponding energy band diagrams (where k and a are the wavevector and lattice constant, respectively) of TLG obtained from the tight-binding calculation. The shaded areas in the diagrams represent the electron-filled regions of the bands, indicating the substrate-induced p-doping at $E_f = -0.07$ eV. The curved orange arrows represent depict intraband transitions. (c) Real (solid curves) and imaginary (dotted curves) parts of optical conductivities of ABA (red) and ABC (blue) TLG at in-plane momentum component of $q = 1/r_{tip}$ (where $r_{tip} = 30$ nm corresponds to the radius of curvature of sSNOM tip). The optical conductivities shown are normalized by unit conductivity of $\sigma_0 = e^2/4\hbar$, where e is the unit charge. The gray shading in (c) indicates the frequency range utilized for SPP mapping.

Figure 1b illustrates the band diagrams for ABA and ABC TLG, obtained through TB-calculation[22, 35-37]. In the presence of a SiO_2 substrate, TLG is typically p-doped due to spontaneous electron transfer from graphene to substrate. This results in a Fermi energy (E_f) ranging from -0.02 to -0.2 eV. With the low level of doping (see the gray shadings in Figure 1b), ABA-TLG has two conduction channels (depicted by curved arrows), while ABC-TLG has only one, leading to a higher intra-band optical conductivity in ABA-TLG compared to ABC-TLG. Figure 1c shows the theoretical intraband optical conductivity spectra of ABA-TLG and ABC TLG at $E_f = -0.07$ eV and an in-plane photon momentum of $q = 1 / 30$ nm^{-1}, relevant to our tip-based near-field measurements using a tip with a 30 nm radius of curvature. In the frequency region pertinent to the near-field measurements (900 – 1000 cm^{-1}, indicated

by the gray shading in Figure 1c), the conductivity of ABA-TLG is ~20 % lager than that of ABC-TLG.

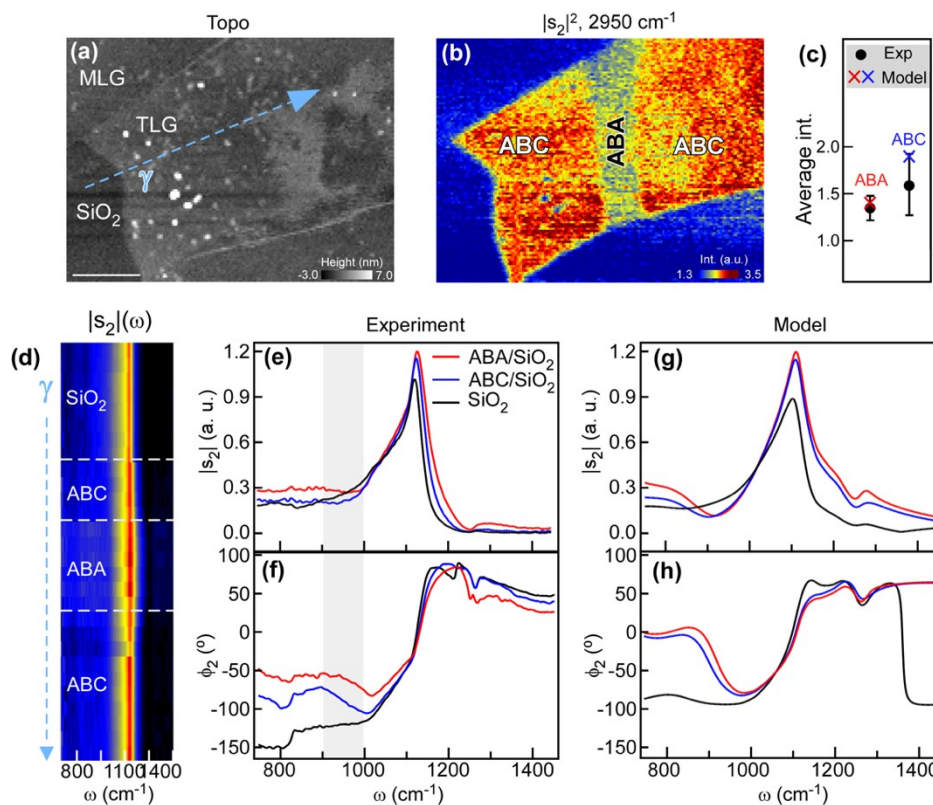### 3.2. Near-field spectroscopy of TLG

Figure 2. (a) AFM topography of the sample, which includes TLG, MLG, and exposed SiO$_2$ substrate. The arrow (γ) in light blue color corresponds to the positions of the sequential line scan of the sSNOM spectrum in (d). The scale bar corresponds to a length of 10 μm. (b) IR-sSNOM intensity image at 2950 cm^{-1} for the sample shown in (a). (c) The average sSNOM intensities of the two TLG domains (black circles) in TLG relative to that of SiO$_2$, derived from (b). Also shown in red and blue crosses are the model sSNOM contrasts of ABA-TLG and ABC-TLG on SiO$_2$. (d) The Fourier-transformed IR-sSNOM spectra of the TLG sample recorded sequentially along the dashed line (γ) shown in (a). (e) & (f) Average IR-sSNOM amplitude (e) and phase (f) spectra of ABA-TLG/SiO$_2$, ABC-TLG/SiO$_2$, and bare SiO$_2$ substrate obtained from (d). In each phase spectrum in (f), ϕ$_2$ at the peak of SiO$_2$ phonon mode is set to zero. Gray shading indicates the frequency window of IR light used for SPP mapping. (g) & (h) Corresponding model IR-sSNOM spectra obtained from the point-dipole model of tip-sample coupling and theoretical conductivities (at E_f = -0.07 eV) shown in Figure 1c.

To indirectly evaluate the stacking-specific intraband conductivities of TLG relevant to SPP measurements, we performed IR-sSNOM spectroscopy on ABA and ABC TLG sample on a SiO$_2$ substrate. Figure 2a depicts an atomic force microscopy (AFM) image (topography)

6

of the TLG on a SiO$_2$ / Si substrate. The stacking domains were identified through IR-sSNOM imaging at 2950 cm^{-1} (Figure 2b). At this IR frequency, the ABC domain appears brighter than the ABA domain due to the pronounced interband optical resonance[22] for ABC-TLG occurring at 2000 - 3000 cm^{-1}. The relative contrasts of the stacking domains and their comparison with the sSNOM contrast model (Figure 2c; Supporting Information 3) further supports the identification of stacking domains.

Figure 2d presents the IR-sSNOM amplitude spectra ($|s_2|(\omega)$) of the same sample sequentially recorded along the dashed line in Figure 2a (denoted as γ). The spectra cover the frequency window of SiO$_2$ phonon resonance and the intraband transition of TLG. Figs. 2e and f display the amplitude ($|s_2|(\omega)$), and phase ($\phi_2(\omega)$) spectra averaged over the regions of SiO$_2$, ABC-TLG/SiO$_2$, and ABA-TLG/SiO$_2$. Similar to the case of MLG on SiO$_2$[4], the presence of TLG on SiO$_2$ leads to a blue-shifts and enhancement of the SiO$_2$ phonon peak in the amplitude spectra. This spectral modification, resulting from the coupling between the plasmon of TLG and the SiO$_2$ phonon, is more pronounced for ABA-TLG than for ABC-TLG. In the frequency range of 934–980 cm^{-1}, where SPP-mapping was performed (see below), the shoulder of SiO$_2$ phonon resonance is still present, causing significant variations in the relative sSNOM amplitudes of ABA-TLG, ABC-TLG, and SiO$_2$ substrate across the frequency window and with the sample's doping condition. The phase spectra (Figure 2f) also exhibit a systematic difference between ABA-TLG and ABC-TLG. This stacking-specific spectral modification can be fully reproduced (Figs. 2g and h) using the point-dipole sSNOM contrast model,[22, 34, 38, 39] based on the empirical dielectric function of SiO$_2$[38] and the TB-calculation derived conductivities of ABA- and ABC-TLG at E_f = -0.07 eV. These findings clearly validate the theoretical stacking-specific conductivities of TLG.

3.3. SPP propagation and reflection in TLG

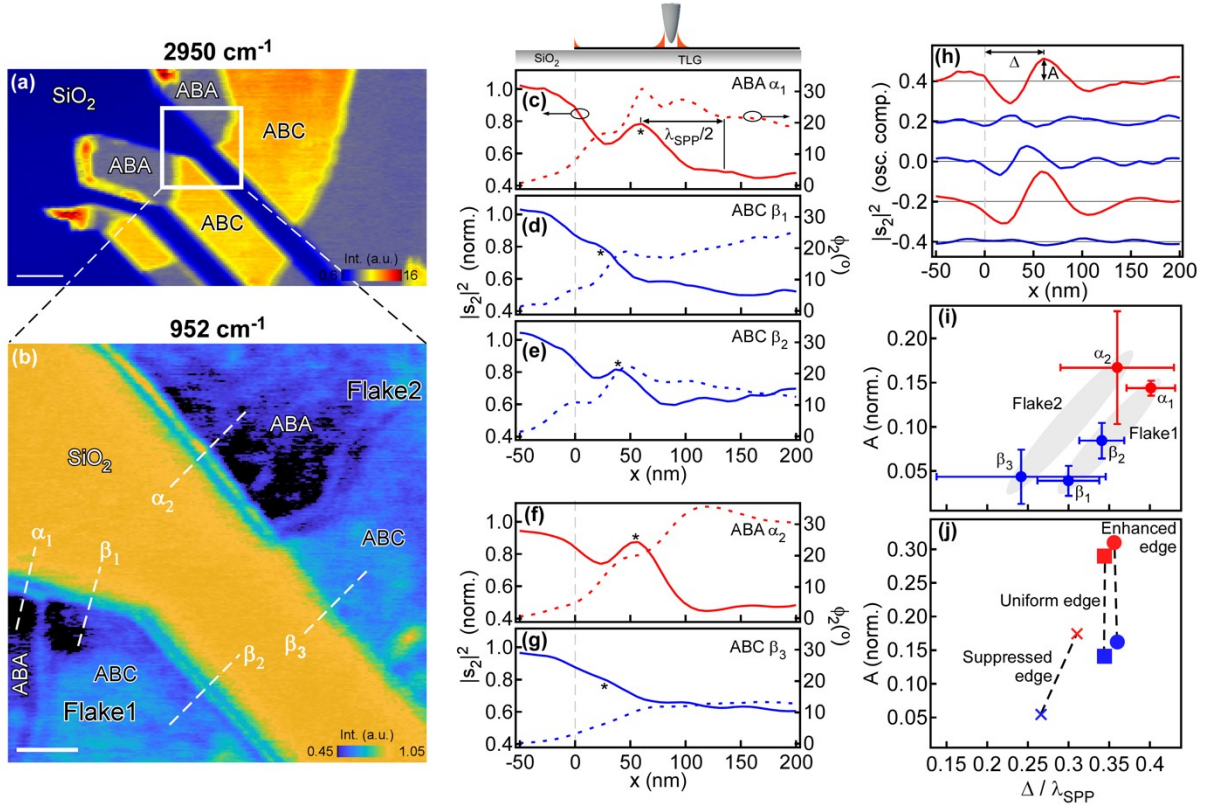**Figure 3**. (a) IR-sSNOM intensity ($|s_2|^2$) image of TLG at 2950 cm^{-1}, where the scale bar corresponds to a length of 1 μm. (b) IR-sSNOM intensity image at 952 cm^{-1}, where the scale bar corresponds to a length of 250 nm. (c)–(e) Line profiles of IR-sSNOM intensity (solid curves) and phase (ϕ_2, dashed curves) sampled at the edges of ABA (red) and ABC (blue) domains along the dashed lines of flake1 of (b). (f) & (g) Corresponding profiles for ABA and ABC domains of flake 2. (h) The oscillating components of the $|s_2|^2$ - profiles shown in (c)-(g), obtained by high-pass signal filtering. The A and Δ represent the amplitude and the location of the first positive fringe peak in the profile, respectively. The traces are vertically displaced for better visibility of the features, with thin solid lines indicating zero amplitude. (i) Plots of (Δ/λ_{SPP}, A) (filled circles in red and blue) derived from the oscillating components of multiple line profiles sampled from five edges containing α_1, α_2, β_1, β_2, and β_3. The error bars indicate one standard deviation in (Δ/λ_{SPP}, A) of multiple line profiles. (j) The (Δ/λ_{SPP}, A)-plot of the modeled SPP profiles for ABA-TLG (red) and ABC-TLG (blue), assuming the models of uniform edge (filled squares), enhanced edge (filled circles, $F = 0.023$ nm^{-1}), and suppressed edge (crosses, $F = -0.046$ nm^{-1}).

Figure 3a shows the IR-sSNOM intensity image of TLG at 2950 cm^{-1}, revealing the ABA (darker) and ABC (brighter) domains of TLG. Figure 3b displays the zoom-in IR-sSNOM scan (marked as a box in Figure 3a) of the sample at 952 cm^{-1}, containing two flakes of TLG (named flake1 and flake2; corresponding topography image is shown in Supporting Information 4). The image shows fringe patterns near the TLG edges and the ABA-ABC

8

boundaries, which represent the interference ($2 \Re\left[\widetilde{\psi}_0 \widetilde{\psi}^{\iota}_r\right]$) between the tip-launched ($\widetilde{\psi}_0$) and reflected ($\widetilde{\psi}_r(2x)$, where x is the distance between the tip and the edge / boundary) SPP waves[1, 2, 7, 13-15, 40, 41]. Figure 3c–g show the sSNOM intensity profiles across the ABA and ABC edges of TLG sampled along the dashed lines indicated in Figure 3b. The y-axes of the plots are normalized to the asymptotic sSNOM intensity signal of SiO_2 substrate away from the edge. Also shown in dotted curves are the corresponding sSNOM phase profiles (ϕ_2). For each profile, the edge position ($x = 0$ nm) is determined by the AFM topography image (Supporting Information 5) to within 10 nm accuracy. The wavelength of SPP, λ_{SPP}, deduced from the peak-to-peak distance ($\lambda_{SPP}/2$) (see Figure 3c) of the two adjacent fringe peaks near the edges of TLG, is found to be stacking dependent, with $\lambda_{SPP}^{ABA} = 161.5 \pm 26.6$ nm and $\lambda_{SPP}^{ABC} = 146.9 \pm 30.6$ nm at $\lambda_0 = 10.5$ µm. This stacking dependence is consistently found in the wavelength range of $\lambda_0 = 10.1 \sim 10.7$ µm (Supporting Information 6) and could be modeled by the theoretical λ_0 - λ_{SPP} dispersion relation that takes into account the presence of substrate.

From the sSNOM image and the line profiles, it is evident that there is a significant edge-to-edge variation in SPP fringes. The most notable observation is that the fringe amplitudes near the edges of ABC-TLG are considerably smaller than those of the neighboring edges of ABA-TLG, even though they share the same linear topographic TLG / SiO_2 boundaries. This difference is apparent in the pairs of profiles of (ABA-α_1, ABC-β_1) and (ABA-α_2, ABC-β_3). Interestingly, within the same ABC-TLG domain, two edges (β_1 and β_2) exhibit noticeably different fringe amplitudes. These edge-specific SPP-fringes cannot be attributed to stacking-specific tip-sample coupling or plasmon-phonon coupling. Instead, they indicate the facet-dependent SPP-reflection. In the following discussion, we refer to the β_1, β_2, and β_3 edges as strongly reflecting (β_2) and weakly reflecting (β_1 and β_2) ABC-edges. We also observe that the

9

distance from the edge to the first positive fringe in the profile (marked as asterisks in Figure 3c-g) is dependent on both the stacking and the facet direction. Specifically, the profiles of ABA-α_1 and α_2 edges show the position of the first peak at $\Delta = 0.36 \cdot \lambda_{SPP}^{ABA}$. The SPP-profiles for the weakly reflecting ABC-edges (β_1 and β_3) show the positions of the first signal maximum at $\Delta = 0.16 \cdot \lambda_{SPP}^{ABC}$, which is positioned closer to edges than that of strongly reflecting ABC-edge at $\Delta = 0.29 \cdot \lambda_{SPP}^{ABC}$. This observation suggests that the SPP reflected from the weakly reflecting ABC-edges has acquired a reflection phase that significantly differs from those of the strongly reflecting ABC-edge and ABA-edge. The sSNOM phase profiles (dotted curves in Figures 4c-g; Supporting Information 4) also exhibit analogous stacking- and edge-specific SPP fringes, providing further evidence. Supporting Information 7 shows a set of TLG sSNOM images of another sample that demonstrate such differences.

To better quantify the stacking- and edge-specific fringe amplitude and fringe position, we have isolated (through high pass signal filtering) the oscillatory components (Figure 3h) from multiple line profiles sampled from five facets of TLG containing α_1, β_1, β_2, α_2, and β_3 lines, and measured the average amplitude (A) and position (Δ) of the first peak from the set of oscillatory components. The results of this analysis, presented as (Δ/λ_{SPP}, A)-plot, are depicted in Figure 3i (here, λ_{SPP} is the SPP-wavelength of ABA or ABC TLG and the error bars represent one standard deviation of the estimates from multiple profiles). The graph clearly demonstrates that the strongly reflecting (β_2) and weakly reflecting (β_1 and β_3) edges of ABC-TLG exhibit clearly distinguishable A and $\varDelta$. Two factors may contribute to the observed edge and stacking-specific SPP profiles. Firstly, the tip-sample near-field coupling, which is influenced by the stacking order in TLG, can lead to varying efficiencies in SPP launching and detection. This factor may contribute to the observed differences in fringe amplitude (A) but is

10

unlikely to account for the variations in fringe position (Δ / λ_{SPP}). Secondly, the local conductivity near the edge of TLG may differ significantly from that of the bulk, resulting in stacking- and facet-dependent variations in both amplitude and fringe position.
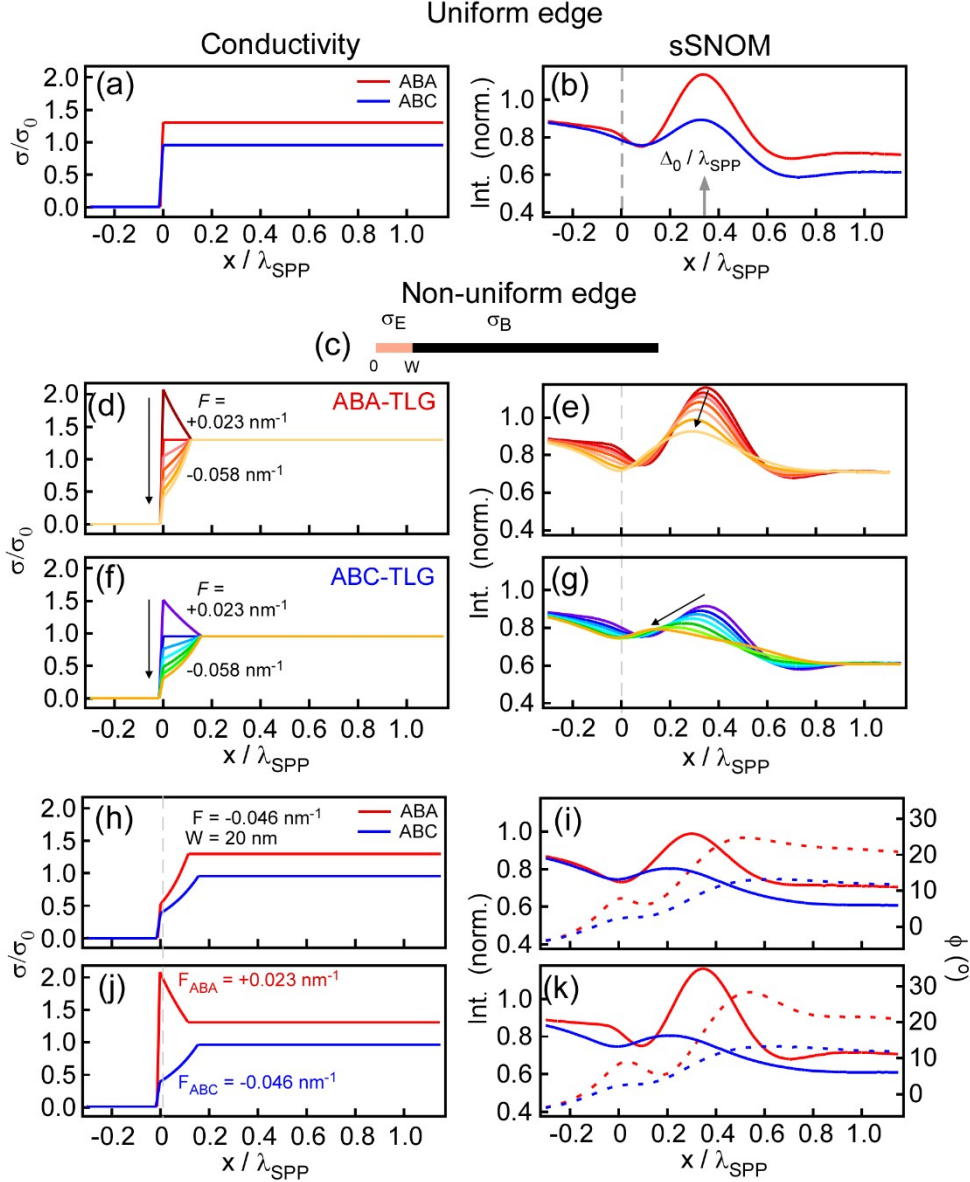

Figure 4. (a) Real parts of the uniform conductivity profiles of ABA (red) and ABC (blue) TLG. (b) Simulated sSNOM intensity profiles based on (a). (d) Non-uniform conductivity models for ABA-TLG with W = 20 nm, F = +0.023 ~ -0.058 nm^{-1}, with the bulk conductivity set to the bulk conductivity of ABA-TLG. (e) The sSNOM intensity profiles derived from (f), shown with the corresponding color. (f) & (g) the same as (d) & (e) but with the bulk conductivity set to that of ABC-TLG. (h) & (i) Edge-suppressed conductivity profiles for ABA and ABC-TLG with the same W and F (values shown in the graph), and the associated sSNOM intensity and phase profile. (j) & (k) Conductivities and sSNOM profiles for the edge-enhanced conductivity for ABA-TLG (F = +0.023 nm^{-1}) and edge-suppressed conductivity for ABC-TLG (F = -0.046 nm^{-1}). The same edge widths of W = 20 nm were used for the two profiles.

Note that the idealized SPP-reflection model[19, 42-44], which assumes a homogeneous conductivity of graphene, predicts the perfect SPP edge-reflection irrespective of its conductivity or dielectric environment.

To investigate these possibilities, we conducted a numerical electrodynamics simulation of sSNOM-detected SPP field at $\lambda_0 = 10.5$ μm, using the method developed by Chen et al[13] (Supporting Information 8). In this simulation, a metallic tip, modeled as a spheroid, was positioned above the sample, the tip-sample junction was illuminated by a plane wave, and the scatted field was evaluated for each lateral position of the tip. Tip-related parameters (such as tip-sample distance, tip-shape, and field sampling position) were adjusted such that the simulated SPP profile of the idealized edge of ABA-TLG closely matches the experimental intensity and phase sSNOM profiles of ABA-TLG (α_1 and α_2). The same set of tip parameters was used for all of modeling the SPP profiles for ABA and ABC TLG.

By employing uniform conductivity profiles for the ABA and ABC edges (as depicted in Figure 4a), we generated two SPP profiles (Figure 4b) that did not exhibit any stacking specificity in terms of fringe position, with $\frac{\Delta_0}{\lambda_{SPP}} = 0.34$. The fringe amplitude ratios of ABA: ABC ~ 2:1 arises from the variation in tip-sample coupling rather than the differences in SPP reflection. While this uniform edge model may explain the differences in (A, Δ / λ_{SPP}) between ABA-TLG and strongly reflecting ABC-TLG (β_2), it fails to account for the fringes observed from weakly reflecting ABC-TLG edges. We propose that the discrepancy can be attributed to the presence of non-uniform conductivity at the edge. Let's consider an edge region with a width of W, where the local conductivity, denoted as σ_E, is different from the bulk conductivity, σ_B (Figure 4c). By employing a simple plane-wave SPP interference model

12

(Supporting Information 9), we can derive the expression for the fringe position, $\frac{\Delta}{\lambda_{SPP}}$, as

follows:

$$\frac{\Delta}{\lambda_{SPP}} = \frac{\Delta_0}{\lambda_{SPP}} + \frac{W}{\lambda_{SPP}} \cdot \frac{\sigma_E - \sigma_B}{\sigma_E}. \tag{1}$$

Here, represents the expected fringe position for a uniform TLG edge. In equation (1), the

term $\frac{W}{\lambda_{SPP}}$ introduces stacking dependence in $\frac{\Delta}{\lambda_{SPP}}$. When the edge conductivity is suppressed

($\sigma_E < \sigma_B$), the fringe is brought closer to the edge. Conversely, when the edge conductivity is

enhanced ($\sigma_E > \sigma_B$¿, the fringe is pushed away from the edge. The effect is more pronounced

in the case of suppressed edge conductivity. Additionally, the fractional change in

conductivity, $\frac{\sigma_E - \sigma_B}{\sigma_E}$, may introduce further stacking-specificity to the SPP fringes.

To further explore such possibility, we conducted numerical sSNOM simulations using

the edge conductivity profile given by:

$$\sigma_E(x) = \sigma_B e^{-F(x-W)}. \tag{2}$$

Here, σ_B represents the bulk conductivities of ABA and ABC TLG, and F is a parameter

describing the cases of edge-enhanced ($F > 0$) or suppressed ($F < 0$) conductivities. The W

denotes the width of the edge region. In Figure 4d and e, we present the simulation results for

ABA-TLG, where the edge conductivity profiles are either enhanced or suppressed. These

profiles not only alter the fringe position but also enhance or suppress the amplitude. Figures

4f and g display an analogous simulation for ABC-TLG using the same F and W parameters.

13

By comparing Figures 4e and g, we find that ABA and ABC TLG with the same suppressed edge conductivity profiles exhibit notably different SPPP profiles.

Based on the simulation, we propose two explanations for the observed stacking and edge specific SPP profiles. Firstly, the stacking-specificity (α_1 versus β_1 and α_2 versus β_3) may be attributed to the presence of step structure at the edges: These step structures arise from the different termination of individual graphene layers within TLG, leading to edge-suppressed conductivity profiles. It is likely that the step structures at the edges of neighboring ABA and ABC domains have similar shapes, resulting in edge conductivity profiles with the same parameters. Through numerical electrodynamics simulations of the edge-suppressed model (Figures 4h and i), where the ABA and ABC domains share parameters of $W = 20$ nm and $F = -0.046$ nm^{-1}, we can reasonably replicate the stacking specificities observed in the sSNOM intensity and phase profiles (Figures 3c, d, f, and g), as well as in (Δ/λ_{SPP}, A) as shown in Figure 3j. Secondly, in addition to the step structures, one of the stacking domains, such as the ABA domain, may support an electronic edge state that enhances the edge conductivity [add reference: Adv. Mater. 2018, 30, 1800367]. This possibility is supported by recent electronic structure calculation[45], which predicts that the edge state of FLG is influenced by both the stacking order and the crystallographic facet. In Figure 4j and k, we present simulation results for this scenario, demonstrating additional stacking specificity in fringe amplitude and position (also seen in Figure 3j). However, the comparison with experimental data does not conclusively determine the significance of the electronic edge state. Nevertheless, the analysis and modeling strongly suggest the presence of non-uniform (potentially suppressed) conductivity at the edges of TLG.
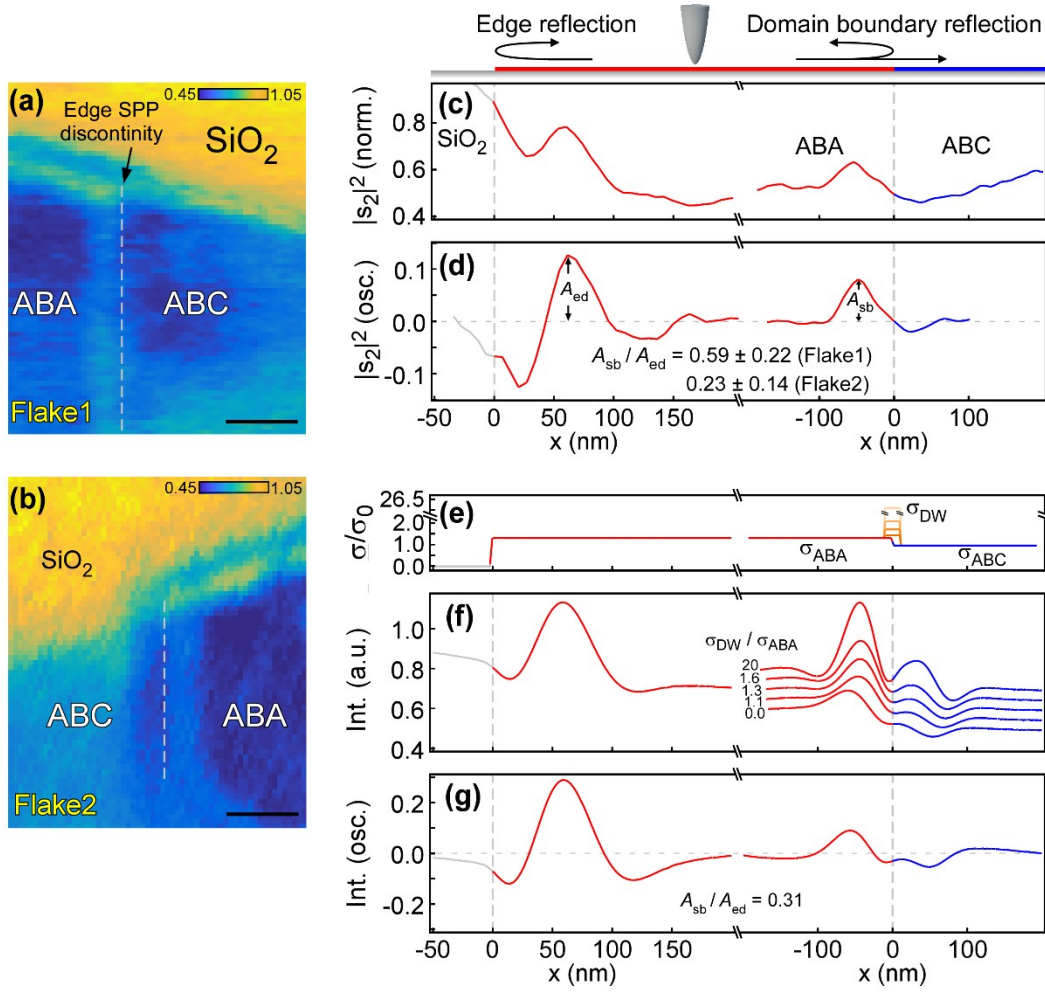
Figure 5. (a) & (b) Zoom-in images of Figure 3b sampled around the ABA-ABC boundaries in flake1 and flake2. Locations of stacking domain boundaries (dashed lines) were determined by the discontinuity in SPP edge-reflection (marked as a black arrow in (a). Scale bar corresponds to 100 nm. (c) The experimental sSNOM intensity ($|s_2|^2$) profile across the domain boundary in (a) (right). Also shown in comparison is the line profile of ABA-TLG edge α_1 (left) obtained from the same domain. (d) The average oscillatory components of profiles across the ABA-ABC boundary in (a) and that of the ABA-TLG α_1 edge. The A_{sb} and A_{ed} in the figure indicate the amplitudes of the first positive fringe peaks at the ABA-side of the stacking domain boundary, and that of the ABA-TLG edge, respectively. The ratios, A_{sb} / A_{ed}, obtained from the flake1 (a) and flake2 (b), represent the relative SPP-reflectivities of the stacking boundary in reference to that of the ABA edge. (e) The conductivity profile for the sSNOM simulation. The domain wall (DW) conductivity is represented as the flat-top-shaped function with the width of $W_{DW} = 20$ nm and the height of $\sigma_{DW} = (0 \sim 20) \times \sigma_{ABA}$. (f) The model sSNOM profiles generated using the conductivity shown in (e). The profiles across the ABA-ABC domain boundary have been vertically displaced to better show the features. (g) The oscillatory components of the simulated profile obtained with $\sigma_{DW} = 0$. Also shown is the corresponding value of A_{sb} / A_{ed}.

Another significant observation is the presence of fringes at the ABA-ABC boundaries (Figure 3b and Figures 5a and b), indicating the partial reflection of SPPs. In the images, the location of boundary ($x = 0$ nm) is determined from the nearby discontinuity in SPP edge

profiles, as indicated by an arrow in Fig. 5a. Figure 5c illustrates a line profile taken across the domain boundary depicted in Figure 5a. For comparison, the line profile of the ABA-α_1 edge from the same domain is also provided. Two noteworthy features can be observed in these profiles. Firstly, the fringe exhibits an asymmetry with respect to the boundary, with a prominent positive peak on the ABA side. The feature qualitatively agrees with the expected behavior of an idealized graphene heterojunction, where a step-like change in conductivity occurs across the domain boundary: Based on the plane-wave model of SPP reflection (Supporting Information 10), such a boundary produces reflected SPP waves of opposite signs on either side of the boundary. Due to the differences in tip-sample coupling on each side, the sSNOM-detected field profile appears asymmetric instead of anti-symmetric. If, on the other hand, SPP reflection is primarily governed by the domain-wall (DW) conductivity, the profile would exhibit a double-peak shape, as observed in SPP profiles across the AB-BA boundary of BLG[7], graphene gap[46], and grain boundary[3, 15]. Secondly, the fringe amplitude of ABA side of the ABA-ABC boundary (A_{sb}) is 20 ~ 60 % of the amplitude at the edge of the same ABA-TLG (A_{ed}), as shown in Figure 5d. The ratio $A_{sb} / A_{ed} = 0.2 \sim 0.6$, which represents the relative SPP-reflectivity of the stacking domain boundary compared to the edge, is in reasonable agreement with the prediction of 0.20 from the plane-wave SPP model for an ideal heterojunction (Supporting Information 10).

To further explore the possible role of DW in SPP reflection, we constructed a conductivity profile (Figure 5e). This profile consists of a rectangular function (width of W_{DW} = 20 nm and the height of $\sigma_{DW} = (0\sim20) \times \sigma_{ABA}$), representing the DW conductivity, added to the step-function profile of an ideal heterojunction. We find that the simulation (see Figures 5f and g) with $\frac{\sigma_{DW}}{\sigma_{ABA}} < ¿2$ can reproduce $A_{sb} / A_{ed} < 0.6$ while maintaining the asymmetric feature

16

of the SPP profile. This indicates that the stacking-domain boundary exhibits behavior similar to that of a near-ideal heterojunction, where the reflection and transmission of SPP are primarily influenced by the conductivities on either side of the boundary.

Overall, the observation provides the physical basis for controlling SPP reflection at stacking domain boundaries. The reflectivity of SPP at the idealized stacking boundary is highly sensitive to the ratio of conductivities of the two domains, and such conductivity ratios may be controlled by electrical doping. The result above clearly demonstrate that stacking domain boundaries offer a near-ideal heterojunction for SPP reflection, with the domain wall playing a marginal role. Our preliminary findings (Supporting Information 11) confirms that the relative sSNOM contrasts and, consequently, the relative conductivity ratios of ABA and ABC domains in TLG can be tuned by applying a back-gate voltage. As such, SPP reflectivity tuning should be possible.

CONCLUSION

Summarizing, we have investigated how the propagation and reflection of SPPs on TLG change with stacking orders. Our observations reveal stacking-dependent near-field scattering spectra and SPP wavelengths, which can be explained by the stacking-dependent intraband conductivities of doped TLG. The reflection of SPPs at ABA-ABC domain boundaries can be attributed to the heterojunction formed by the conductivity discontinuity between the ABA and ABC domains, with the domain wall playing a marginal role. Since the optical conductivity difference between ABA and ABC FLG is dependent on the doping level, the stacking domain boundaries could serve as continuously tunable SPP reflectors for graphene-based optoelectronic devices. Furthermore, we have discovered that the edges of TLG exhibit

17

prominent stacking-specific reflection. These characteristics can be attributed to the presence of local edge conductivity originating from either the step-structure or the electronic edge state. Further sSNOM-based studies of SPPs holds the potential to provide detailed insights into the structure and optical properties of stacking domain boundaries, as well as the behavior of edge states in few-layer graphene.

ASSOCIATED CONTENT

Supporting Information.

Raman spectra of TLG; Optical conductivities calculation; Details of IR-sSNOM spectra modeling; Dispersion curves calculations; Explanation for position-zero (x=0) determination; IR-sSNOM images of various samples; FDTD simulation details; Local edge conductivity model; SPP reflection model at domain wall; Dielectric contrast control;

The Supporting Information is available free of charge at xxxx.

AUTHOR INFORMATION

Corresponding Authors

Zee Hwan Kim, Professor,

Department of Chemistry, Seoul National University, Seoul 08826, Republic of Korea

Email: zhkim@snu.ac.kr

ACKNOWLEDGMENT

REFERENCES

(1) Fei, Z.; Rodin, A. S.; Andreev, G. O.; Bao, W.; McLeod, A. S.; Wagner, M.; Zhang, L. M.; Zhao, Z.; Thiemens, M.; Dominguez, G.; et al. Gate-tuning of graphene plasmons revealed by infrared nano-imaging. *Nature* **2012**, *487* (7405), 82-85. DOI: 10.1038/nature11253.

(2) Ni, G. X.; Wang, L.; Goldflam, M. D.; Wagner, M.; Fei, Z.; McLeod, A. S.; Liu, M. K.; Keilmann, F.; Özyilmaz, B.; Castro Neto, A. H.; et al. Ultrafast optical switching of infrared plasmon polaritons in high-mobility graphene. *Nat. Photon.* **2016**, *10* (4), 244-247. DOI: 10.1038/nphoton.2016.45.

(3) Fei, Z.; Rodin, A. S.; Gannett, W.; Dai, S.; Regan, W.; Wagner, M.; Liu, M. K.; McLeod, A. S.; Dominguez, G.; Thiemens, M.; et al. Electronic and plasmonic phenomena at graphene grain boundaries. *Nat. Nanotechnol.* **2013**, *8* (11), 821-825. DOI: 10.1038/nnano.2013.197.

(4) Fei, Z.; Andreev, G. O.; Bao, W.; Zhang, L. M.; McLeod, A. S.; Wang, C.; Stewart, M. K.; Zhao, Z.; Dominguez, G.; Thiemens, M.; et al. Infrared Nanoscopy of Dirac Plasmons at the Graphene–SiO2 Interface. *Nano Lett.* **2011**, *11* (11), 4701-4705. DOI: 10.1021/nl202362d.

(5) Luan, Y.; Qian, J.; Kim, M.; Ho, K.-M.; Shi, Y.; Li, Y.; Wang, C.-Z.; Tringides, M. C.; Fei, Z. Imaging Stacking-Dependent Surface Plasmon Polaritons in Trilayer Graphene. *Phys. Rev. Appl.* **2022**, *18* (2), 024052. DOI: 10.1103/PhysRevApplied.18.024052.

(6) Chen, J.; Badioli, M.; Alonso-González, P.; Thongrattanasiri, S.; Huth, F.; Osmond, J.; Spasenović, M.; Centeno, A.; Pesquera, A.; Godignon, P.; et al. Optical nano-imaging of gate-tunable graphene plasmons. *Nature* **2012**, *487* (7405), 77-81. DOI: 10.1038/nature11254.

(7) Jiang, L.; Shi, Z.; Zeng, B.; Wang, S.; Kang, J.-H.; Joshi, T.; Jin, C.; Ju, L.; Kim, J.; Lyu, T.; et al. Soliton-dependent plasmon reflection at bilayer graphene domain walls. *Nat. Mater.* **2016**, *15* (8), 840-844. DOI: 10.1038/nmat4653.

(8) Fei, Z.; Foley, J. J. I.; Gannett, W.; Liu, M. K.; Dai, S.; Ni, G. X.; Zettl, A.; Fogler, M. M.; Wiederrecht, G. P.; Gray, S. K.; et al. Ultraconfined Plasmonic Hotspots Inside Graphene Nanobubbles. *Nano Lett.* **2016**, *16* (12), 7842-7848. DOI: 10.1021/acs.nanolett.6b04076.

(9) Hu, F.; Luan, Y.; Fei, Z.; Palubski, I. Z.; Goldflam, M. D.; Dai, S.; Wu, J. S.; Post, K. W.; Janssen, G. C. A. M.; Fogler, M. M.; et al. Imaging the Localized Plasmon Resonance Modes in Graphene Nanoribbons. *Nano Lett.* **2017**, *17* (9), 5423-5428. DOI: 10.1021/acs.nanolett.7b02029.

(10) Hu, H.; Yang, X.; Zhai, F.; Hu, D.; Liu, R.; Liu, K.; Sun, Z.; Dai, Q. Far-field nanoscale infrared spectroscopy of vibrational fingerprints of molecules with graphene plasmons. *Nat. Commun.* **2016**, *7* (1), 12334. DOI: 10.1038/ncomms12334.

(11) Rodrigo, D.; Limaj, O.; Janner, D.; Etezadi, D.; García de Abajo, F. J.; Pruneri, V.; Altug, H. Mid-infrared plasmonic biosensing with graphene. *Science* **2015**, *349* (6244), 165-168. DOI: 10.1126/science.aab2051 (acccessed 2022/12/20).

(12) Nikitin, A. Y.; Guinea, F.; García-Vidal, F. J.; Martín-Moreno, L. Edge and waveguide terahertz surface plasmon modes in graphene microribbons. *Phys. Rev. B* **2011**, *84* (16), 161407. DOI: 10.1103/PhysRevB.84.161407.

(13) Chen, J.; Nesterov, M. L.; Nikitin, A. Y.; Thongrattanasiri, S.; Alonso-González, P.; Slipchenko, T. M.; Speck, F.; Ostler, M.; Seyller, T.; Crassee, I.; et al. Strong Plasmon

Reflection at Nanometer-Size Gaps in Monolayer Graphene on SiC. *Nano Lett.* **2013**, *13* (12), 6210-6215. DOI: 10.1021/nl403622t.

(14) Kang, J.-H.; Wang, S.; Shi, Z.; Zhao, W.; Yablonovitch, E.; Wang, F. Goos-Hänchen Shift and Even–Odd Peak Oscillations in Edge-Reflections of Surface Polaritons in Atomically Thin Crystals. *Nano Lett.* **2017**, *17* (3), 1768-1774. DOI: 10.1021/acs.nanolett.6b05077.

(15) Gerber, J. A.; Berweger, S.; O'Callahan, B. T.; Raschke, M. B. Phase-Resolved Surface Plasmon Interferometry of Graphene. *Phys. Rev. Lett.* **2014**, *113* (5), 055502. DOI: 10.1103/PhysRevLett.113.055502.

(16) Ju, L.; Shi, Z.; Nair, N.; Lv, Y.; Jin, C.; Velasco, J.; Ojeda-Aristizabal, C.; Bechtel, H. A.; Martin, M. C.; Zettl, A.; et al. Topological valley transport at bilayer graphene domain walls. *Nature* **2015**, *520* (7549), 650-655. DOI: 10.1038/nature14364.

(17) Castilla, S.; Terrés, B.; Autore, M.; Viti, L.; Li, J.; Nikitin, A. Y.; Vangelidis, I.; Watanabe, K.; Taniguchi, T.; Lidorikis, E.; et al. Fast and Sensitive Terahertz Detection Using an Antenna-Integrated Graphene pn Junction. *Nano Lett.* **2019**, *19* (5), 2765-2773. DOI: 10.1021/acs.nanolett.8b04171.

(18) Voronin, K. V.; Aseguinolaza Aguirreche, U.; Hillenbrand, R.; Volkov, V. S.; Alonso-González, P.; Nikitin, A. Y. Nanofocusing of acoustic graphene plasmon polaritons for enhancing mid-infrared molecular fingerprints. *Nanophotonics* **2020**, *9* (7), 2089-2095. DOI: doi:10.1515/nanoph-2020-0164 (acccessed 2022-10-28).

(19) Rejaei, B.; Khavasi, A. Scattering of surface plasmons on graphene by a discontinuity in surface conductivity. *J. Opt.* **2015**, *17* (7), 075002. DOI: 10.1088/2040-8978/17/7/075002.

(20) Jiang, B.-Y.; Mele, E. J.; Fogler, M. M. Theory of plasmon reflection by a 1D junction. *Opt. Express* **2018**, *26* (13), 17209-17226. DOI: 10.1364/OE.26.017209.

(21) Jiang, X.; Luo, W.; Zhang, N.; Fan, J.; Wang, L.; Xiang, Y.; Lu, Y.; Ma, Z.; Ren, M.; Zhang, X.; et al. In-plane reflection phase engineering of graphene plasmons realized by electronic boundary design at the nanoscale. *AIP Adv.* **2022**, *12* (1), 015108. DOI: 10.1063/5.0081395 (acccessed 2022/12/21).

(22) Kim, D.-S.; Kwon, H.; Nikitin, A. Y.; Ahn, S.; Martín-Moreno, L.; García-Vidal, F. J.; Ryu, S.; Min, H.; Kim, Z. H. Stacking Structures of Few-Layer Graphene Revealed by Phase-Sensitive Infrared Nanoscopy. *ACS Nano* **2015**, *9* (7), 6765-6773. DOI: 10.1021/acsnano.5b02813.

(23) Khodkov, T.; Withers, F.; Christopher Hudson, D.; Felicia Craciun, M.; Russo, S. Electrical transport in suspended and double gated trilayer graphene. *Appl. Phys. Lett.* **2012**, *100* (1), 013114. DOI: 10.1063/1.3675337 (acccessed 2022/12/20).

(24) Khodkov, T.; Khrapach, I.; Craciun, M. F.; Russo, S. Direct Observation of a Gate Tunable Band Gap in Electrical Transport in ABC-Trilayer Graphene. *Nano Lett.* **2015**, *15* (7), 4429-4433. DOI: 10.1021/acs.nanolett.5b00772.

(25) Zou, K.; Zhang, F.; Clapp, C.; MacDonald, A. H.; Zhu, J. Transport Studies of Dual-Gated ABC and ABA Trilayer Graphene: Band Gap Opening and Band Structure Tuning in Very Large Perpendicular Electric Fields. *Nano Lett.* **2013**, *13* (2), 369-373. DOI: 10.1021/nl303375a.

(26) Bao, W.; Jing, L.; Velasco, J.; Lee, Y.; Liu, G.; Tran, D.; Standley, B.; Aykol, M.; Cronin, S. B.; Smirnov, D.; et al. Stacking-dependent band gap and quantum transport in trilayer graphene. *Nat. Phys.* **2011**, *7* (12), 948-952. DOI: 10.1038/nphys2103.

(27) Jhang, S. H.; Craciun, M. F.; Schmidmeier, S.; Tokumitsu, S.; Russo, S.; Yamamoto, M.; Skourski, Y.; Wosnitza, J.; Tarucha, S.; Eroms, J.; et al. Stacking-order dependent transport properties of trilayer graphene. *Phys. Rev. B* **2011**, *84* (16), 161408. DOI:

10.1103/PhysRevB.84.161408.

(28) Qian, J.; Luan, Y.; Kim, M.; Ho, K.-M.; Shi, Y.; Wang, C.-Z.; Li, Y.; Fei, Z. Nonequilibrium phonon tuning and mapping in few-layer graphene with infrared nanoscopy. *Phys. Rev. B* **2021**, *103* (20), L201407. DOI: 10.1103/PhysRevB.103.L201407.

(29) Wirth, K. G.; Hauck, J. B.; Rothstein, A.; Kyoseva, H.; Siebenkotten, D.; Conrads, L.; Klebl, L.; Fischer, A.; Beschoten, B.; Stampfer, C.; et al. Experimental Observation of ABCB Stacked Tetralayer Graphene. *ACS Nano* **2022**, *16* (10), 16617-16623. DOI: 10.1021/acsnano.2c06053.

(30) Lui, C. H.; Li, Z.; Mak, K. F.; Cappelluti, E.; Heinz, T. F. Observation of an electrically tunable band gap in trilayer graphene. *Nat. Phys.* **2011**, *7* (12), 944-947. DOI: 10.1038/nphys2102.

(31) Lui, C. H.; Cappelluti, E.; Li, Z.; Heinz, T. F. Tunable Infrared Phonon Anomalies in Trilayer Graphene. *Phys. Rev. Lett.* **2013**, *110* (18), 185504. DOI: 10.1103/PhysRevLett.110.185504.

(32) Bechtel, H. A.; Muller, E. A.; Olmon, R. L.; Martin, M. C.; Raschke, M. B. Ultrabroadband infrared nanospectroscopic imaging. *Proc. Natl. Acad. Sci. U.S.A.* **2014**, *111* (20), 7191-7196. DOI: 10.1073/pnas.1400502111 (acccessed 2023/03/06).

(33) Bechtel, H. A.; Johnson, S. C.; Khatib, O.; Muller, E. A.; Raschke, M. B. Synchrotron infrared nano-spectroscopy and -imaging. *Surf. Sci. Rep.* **2020**, *75* (3), 100493. DOI: https://doi.org/10.1016/j.surfrep.2020.100493.

(34) Jeong, G.; Choi, B.; Kim, D.-S.; Ahn, S.; Park, B.; Kang, J. H.; Min, H.; Hong, B. H.; Kim, Z. H. Mapping of Bernal and non-Bernal stacking domains in bilayer graphene using infrared nanoscopy. *Nanoscale* **2017**, *9* (12), 4191-4195, 10.1039/C7NR00713B. DOI: 10.1039/C7NR00713B.

(35) Zhang, F.; Sahu, B.; Min, H.; MacDonald, A. H. Band structure of ABC-stacked graphene trilayers. *Phys. Rev. B* **2010**, *82* (3), 035409. DOI: 10.1103/PhysRevB.82.035409.

(36) Luxmoore, I. J.; Gan, C. H.; Liu, P. Q.; Valmorra, F.; Li, P.; Faist, J.; Nash, G. R. Strong Coupling in the Far-Infrared between Graphene Plasmons and the Surface Optical Phonons of Silicon Dioxide. *ACS Photonics* **2014**, *1* (11), 1151-1155. DOI: 10.1021/ph500233s.

(37) Jang, Y.; Hwang, E. H.; MacDonald, A. H.; Min, H. Stacking dependence of carrier interactions in multilayer graphene systems. *Phys. Rev. B* **2015**, *92* (4), 041411. DOI: 10.1103/PhysRevB.92.041411.

(38) Kischkat, J.; Peters, S.; Gruska, B.; Semtsiv, M.; Chashnikova, M.; Klinkmüller, M.; Fedosenko, O.; Machulik, S.; Aleksandrova, A.; Monastyrskyi, G.; et al. Mid-infrared optical properties of thin films of aluminum oxide, titanium dioxide, silicon dioxide, aluminum nitride, and silicon nitride. *Appl. Opt.* **2012**, *51* (28), 6789-6798. DOI: 10.1364/AO.51.006789.

(39) Knoll, B.; Keilmann, F. Enhanced dielectric contrast in scattering-type scanning near-field optical microscopy. *Opt. Commun.* **2000**, *182* (4), 321-328. DOI: https://doi.org/10.1016/S0030-4018(00)00826-9.

(40) Wang, X.; Zheng, Z.; Xu, N.; Wang, W.; Chen, H.; Deng, S. A Nano-Imaging Study of Graphene Edge Plasmons with Chirality-Dependent Dispersions. *Adv. Opt. Mater.* **2021**, *9* (10), 2100207, https://doi.org/10.1002/adom.202100207. DOI: https://doi.org/10.1002/adom.202100207 (acccessed 2022/12/21).

(41) Woessner, A.; Lundeberg, M. B.; Gao, Y.; Principi, A.; Alonso-González, P.; Carrega, M.; Watanabe, K.; Taniguchi, T.; Vignale, G.; Polini, M.; et al. Highly confined low-loss plasmons in graphene–boron nitride heterostructures. *Nat. Mater.* **2015**, *14* (4), 421-425.

DOI: 10.1038/nmat4169.

(42) Garcia-Pomar, J. L.; Nikitin, A. Y.; Martin-Moreno, L. Scattering of Graphene Plasmons by Defects in the Graphene Sheet. *ACS Nano* **2013**, *7* (6), 4988-4994. DOI: 10.1021/nn400342v.

(43) Du, L.; Tang, D.; Yuan, X. Edge-reflection phase directed plasmonic resonances on graphene nano-structures. *Opt. Express* **2014**, *22* (19), 22689-22698. DOI: 10.1364/OE.22.022689.

(44) Nikitin, A. Y.; Low, T.; Martin-Moreno, L. Anomalous reflection phase of graphene plasmons and its influence on resonators. *Phys. Rev. B* **2014**, *90* (4), 041407. DOI: 10.1103/PhysRevB.90.041407.

(45) Jung, J.; Zhang, F.; Qiao, Z.; MacDonald, A. H. Valley-Hall kink and edge states in multilayer graphene. *Phys. Rev. B* **2011**, *84* (7), 075418. DOI: 10.1103/PhysRevB.84.075418.

(46) Xu, Q.; Ma, T.; Danesh, M.; Shivananju, B. N.; Gan, S.; Song, J.; Qiu, C.-W.; Cheng, H.-M.; Ren, W.; Bao, Q. Effects of edge on graphene plasmons as revealed by infrared nanoimaging. *Light Sci. Appl.* **2017**, *6* (2), e16204-e16204. DOI: 10.1038/lsa.2016.204.